Electronic Supplementary Material (ESI) for Energy & Environmental Science.

Thermal Instability Originating from the Interface between Organic-Inorganic Hybrid Perovskite and Oxide Electron Transport layers

Jingsi Song,[a#] Hongpeng Liu,[a#] Wenhua Pu,[b#] Yue Lu,[a*] Zhixiang Si,[a] Zeyu Zhang,[a] Yang Ge,[a] Nengxu Li,[c] Huanping Zhou,[c] Wei Xiao,[b*] Ligen Wang,[b] Manling Sui[a*]

[a]Beijing Key Laboratory of Microstructure and Properties of Solids, Faculty of Materials and Manufacturing, Institute of Microstructure and Properties of Advanced Materials, Beijing University of Technology, Beijing, 100124, China.

[b]State Key Laboratory of Nonferrous Metals and Processes, GRIMAT Group Co., Ltd; GRIMAT Engineering Institute Co., Ltd., Beijing 100088, China

[c]Beijing Key Laboratory for Theory and Technology of Advanced Battery Materials, Key Laboratory of Polymer Chemistry and Physics of Ministry of Education, BIC-ESAT, Department of Materials Science and Engineering, College of Engineering, Peking University, Beijing 100871, P.R. China.

# These authors are eco-contribution.

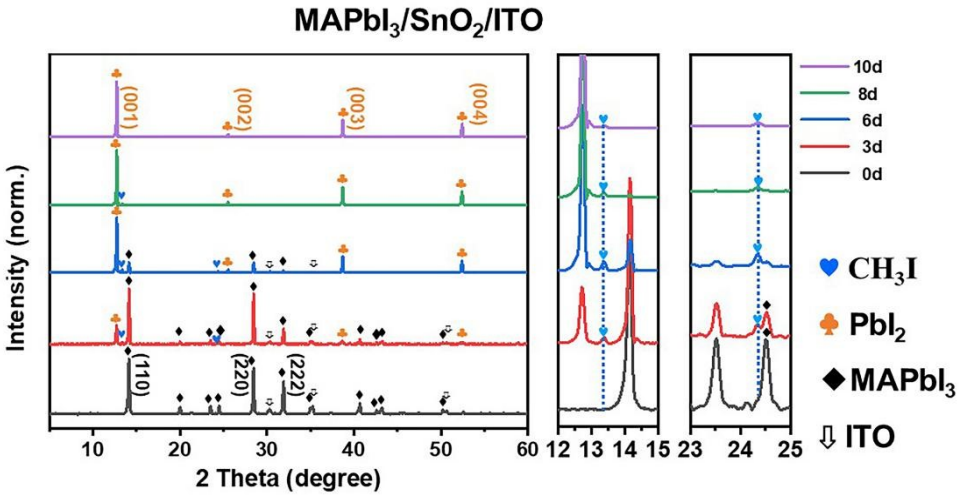

Fig. S1 X-Ray diffraction pattern analyses of the $MAPbI_3$ films on the SnO_2-ITO substrate after thermal treatment for different times. The black indexes correspond to the structure of the tetragonal perovskite and the orange indexes correspond to the structure of lead iodide. Magnified images for the regions of 12~15 degrees and 23~25 degrees were presented on the right side to show the peaks of CH_3I-like phase. The PbI_2 could be characterized as 2H-PbI_2 (space group: $P\bar{3}m1$, a=b=4.558Å, c=6.986Å).

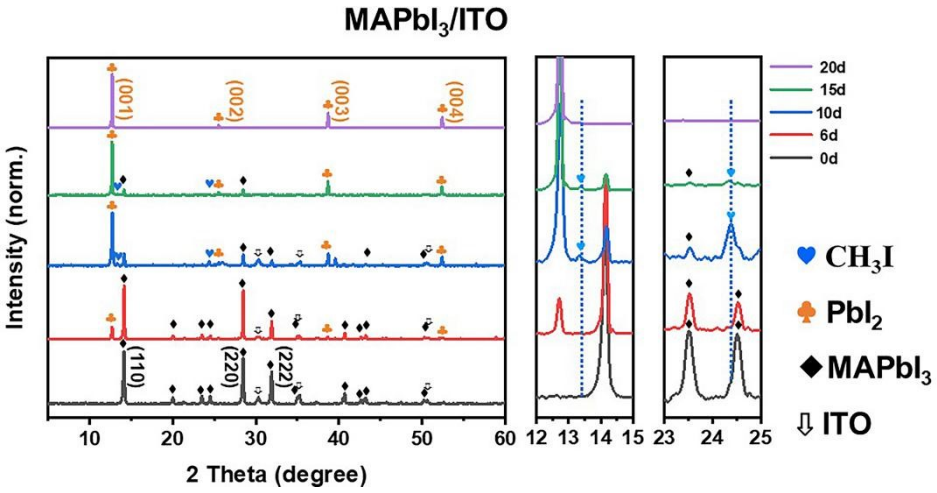

Fig. S2 X-Ray diffraction pattern analyses of the $MAPbI_3$ films on ITO substrates after thermal treatment. The degradation process of $MAPbI_3$ film is very similar to the ones on SnO_2-ITO glasses.

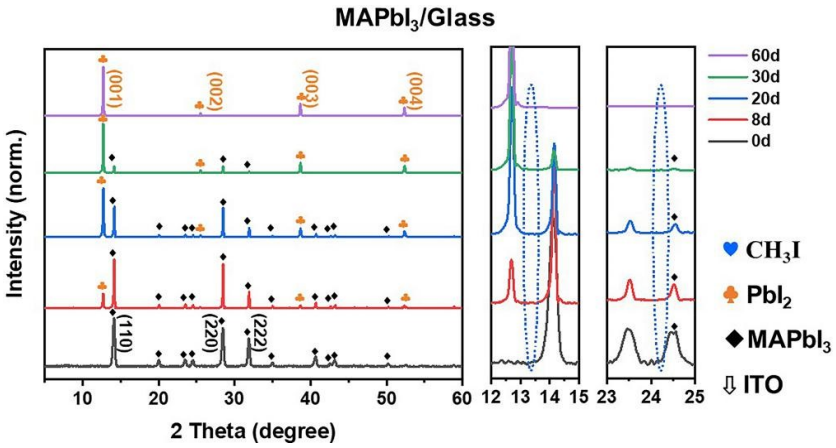

Fig. S3 X-Ray diffraction pattern analyses of the thermal treated $MAPbI_3$ films on the bare glass. The degradation process from $MAPbI_3$ into PbI_2 is similar to the ones on SnO_2-ITO and ITO glasses, but there is no CH_3I-like phase generated.

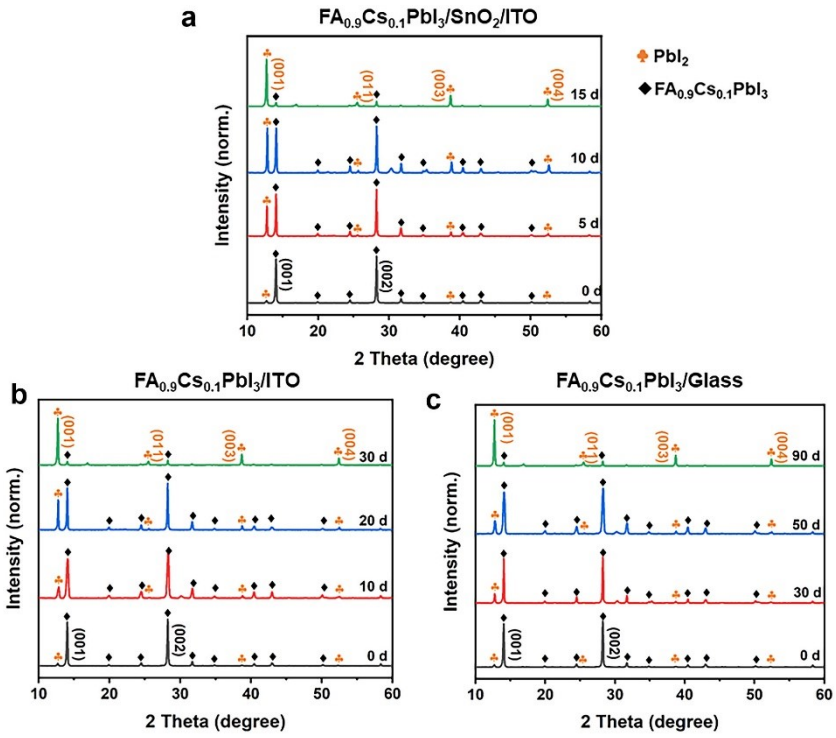

Fig. S4 Evolution for the crystal structures of $FA_{0.9}Cs_{0.1}PbI_3$ films during thermal treatment on SnO_2-ITO, ITO and bare glass substrates, respectively. a-c) X-Ray diffraction patterns analyses on the $FA_{0.9}Cs_{0.1}PbI_3$ films on (a) SnO_2-ITO, (b) ITO and (c) bare glass substrates after thermal treatment for different times. The black indexes correspond to the structure of the cubic perovskite and the orange indexes correspond to the structure of lead iodide.

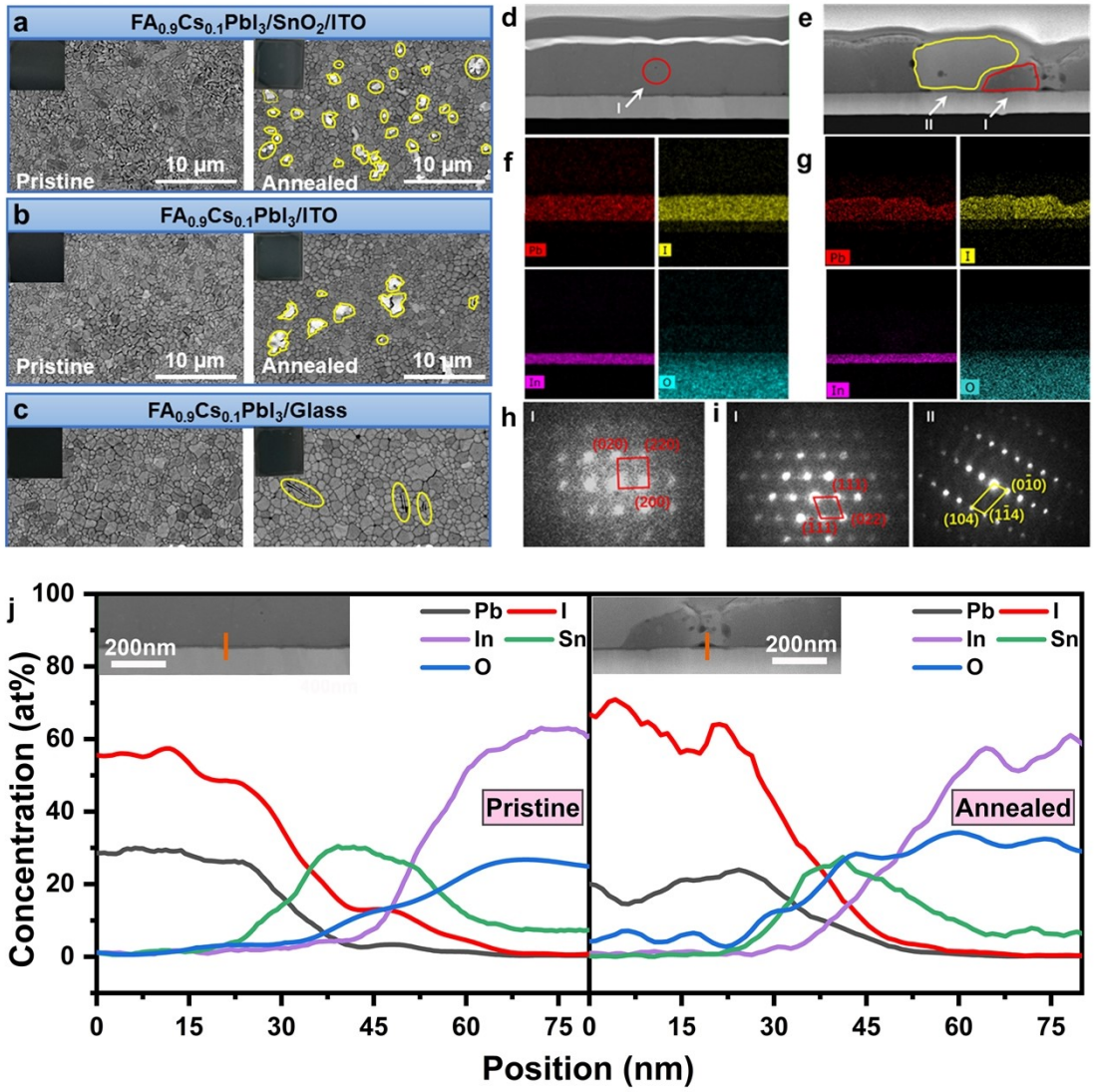

Fig. S5 SEM and TEM observation for the morphology, structure and elementary evolution of the annealed perovskite films on the different substrates. a-c) SEM characterizations of the morphology evolution of spin-coated $FA_{0.9}Cs_{0.1}PbI_3$ perovskite films before and after thermal treatment for 3 days on three different substrates of SnO_2-ITO glass (**a**), ITO glass (**b**) and bare glass (**c**), respectively. Insets show the optical images of the films. Yellow polygon areas indicate the PbI_2 grains. **d, e)** HAADF images of the perovskite films on the SnO_2-ITO glass after thermal degradation for 0 and 3 days, respectively. Red and yellow polygon areas indicate the $FA_{0.9}Cs_{0.1}PbI_3$ and PbI_2 grains. **f, g)** EDS mapping of the cross-sectional perovskite films on SnO_2-ITO glasses after thermal degradation for 0 and 3 days, respectively. **h, i)** NBD patterns of the perovskite films on SnO_2-ITO glass, which are captured at the areas I (red area) and II (yellow area) in **d, e**. **j)** The EDS line scan of the elementary distributions along the

red lines at the interfaces (insets of the HAADF images of the detail interface) between $FA_{0.9}Cs_{0.1}PbI_3$ and SnO_2.

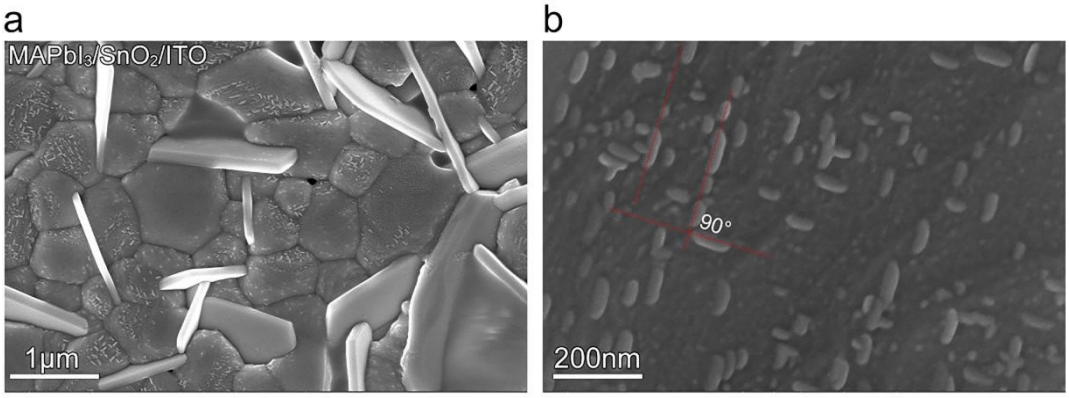

Fig. S6 SEM image of the $MAPbI_3$ film after thermal treatment of 8 days. Except for the appearance of flaky PbI_2 grains at the grain boundaries of perovskite, large number of fine lead iodide grains have been grown out of the surface of $MAPbI_3$ film, which are with a certain crystallographic angle of about 90 degree.

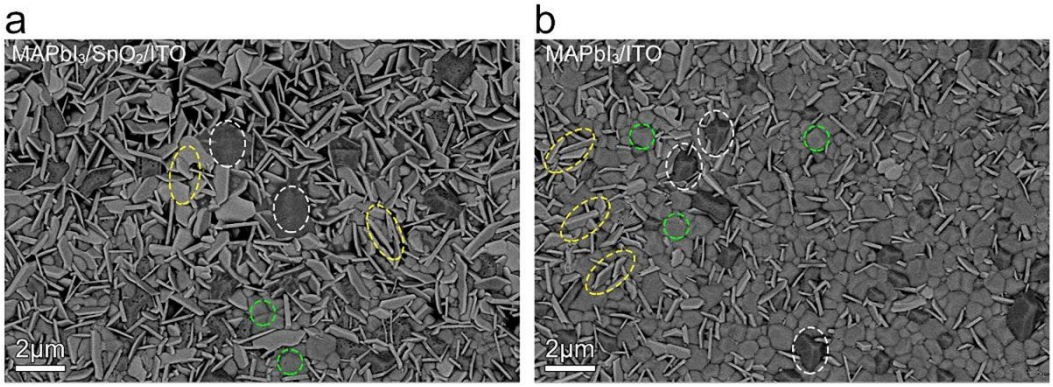

Fig. S7 Top-view back scattered electron (BSE) images of the annealed $MAPbI_3$ films fabricated on the SnO_2-ITO and ITO glass substrates, respectively. The contrast of the BSE images is proportional to the average atomic number of materials. So, as shown in **a** and **b**, the dark contrast of the nanograins (marked with white dash circles) indicates its containing of light elements, which corresponds to the CH_3I-like phase as shown in Figs. S1 and S2. While the flaky grains are PbI_2 (marked with yellow dash circles) and the other grains are with $MAPbI_3$ phase (marked with green dash circles). All the films were thermally treated at 85 °C for 8 days.

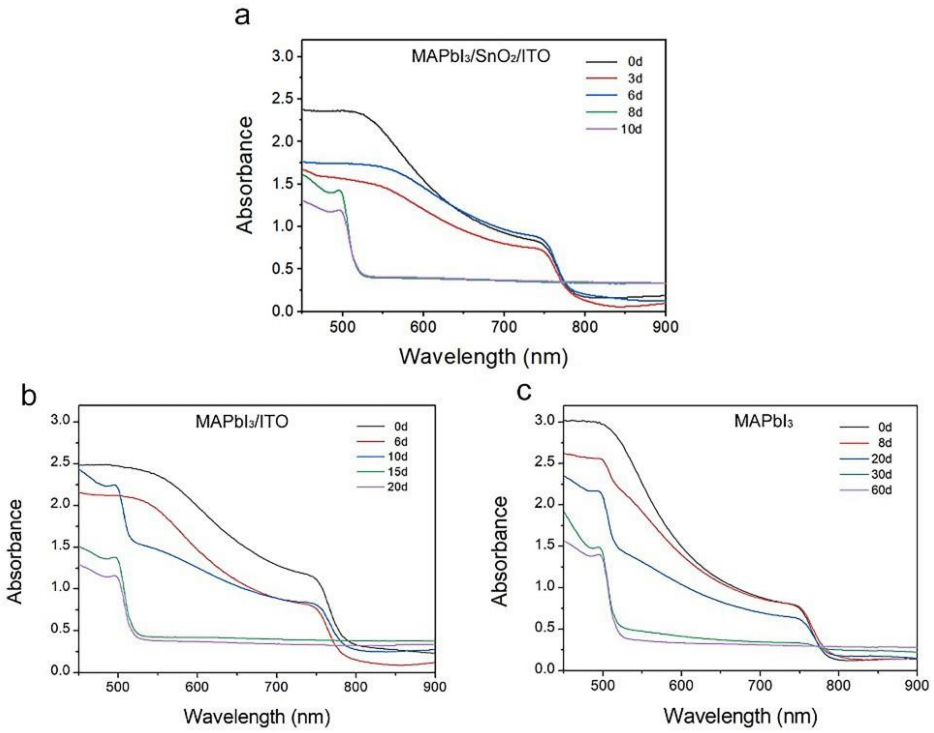

Fig. S8 UV-vis absorbance spectra of the thermally treated $MAPbI_3$ Perovskite film on SnO_2-ITO, ITO and glass substrates, respectively. The absorption characteristics of perovskite $MAPbI_3$ is at 750 nm and lead iodide is at 500 nm, all of these data exhibit the transformation from perovskite into lead iodide.

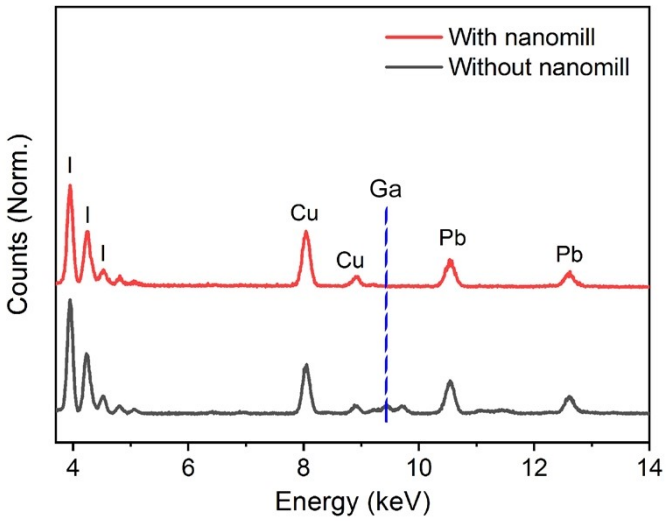

Fig. S9 The EDS spectra of the $MAPbI_3$ layer before and after the nanomill treatment. The FIB-SEM prepared perovskite samples were ion cleaned by Fischione's Model 1040 Nanomill, which can effectively eliminate the damage of Ga ion on the sample surface layer. After slicing the samples, the thickness of them is about 0.25 μm.

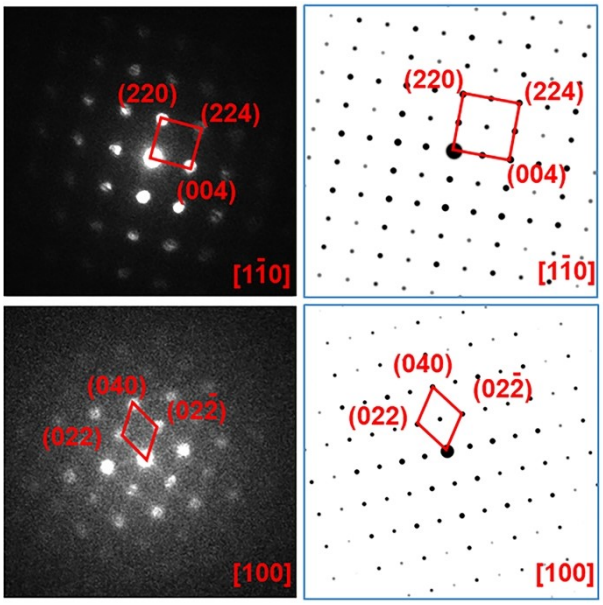

Fig. S10 NBD patterns of the $MAPbI_3$ film. a, b) The NBD pattern could be identified as tetragonal perovskite along [$1\bar{1}0$] zone axis. However, comparing with the simulation result, (110) and (002) diffraction spots become dimmer. **c, d)** Another NBD pattern should be tetragonal perovskite along [100] zone axis, but with the extinction of (110) diffraction spot. All the dim diffraction spots maybe resulted by beam damage of defect generation[63]. It should point out that, all the NBD patterns could not be characterized as 6H-PbI_2 (space group: $R\bar{3}m$, a =b = 4.557 Å, c = 20.937 Å) or 2H-PbI_2 (space group: $P\bar{3}m1$, a=b=4.558 Å, c=6.986 Å).

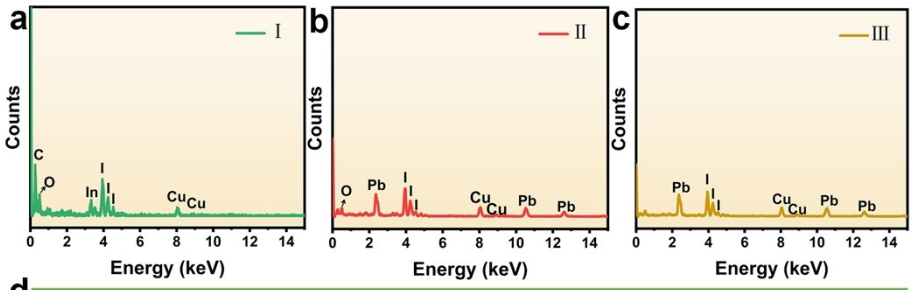

d

Sample	$MAPbI_3$/ITO			$MAPbI_3/SnO_2$/ITO		
District Elements	Ⅰ(at%)	Ⅱ(at%)	Ⅲ(at%)	Ⅰ(at%)	Ⅱ(at.)	Ⅲ(at.)
Pb	1.1	23.8	31.4	0.9	24.2	32.7
I	76.7	65.4	67.1	80.0	66.2	65.7
O	8.6	6.2	1.2	12.4	5.3	1.4
In	13.6	4.6	0.3	6.7	4.3	0.2

Fig. S11 Representative EDS spectra at I-III areas. **a-c)** EDS spectra for I-III areas (I CH_3I-like solid phase, II $MAPbI_3$, III PbI_2) of Fig. 2e. **d)** Table for the element concentration at the regions I-III in the HAADF images of Fig. 2d and Fig. 2e. Region I marked the amorphous CH_3I region, which contained extremely high concentration of iodine, carbon and oxygen elements. Region II marked the perovskite grains for element mapping. Region III shows a flaky lead-iodine grains with the content ratio close to 1:2 for lead and iodine elements.

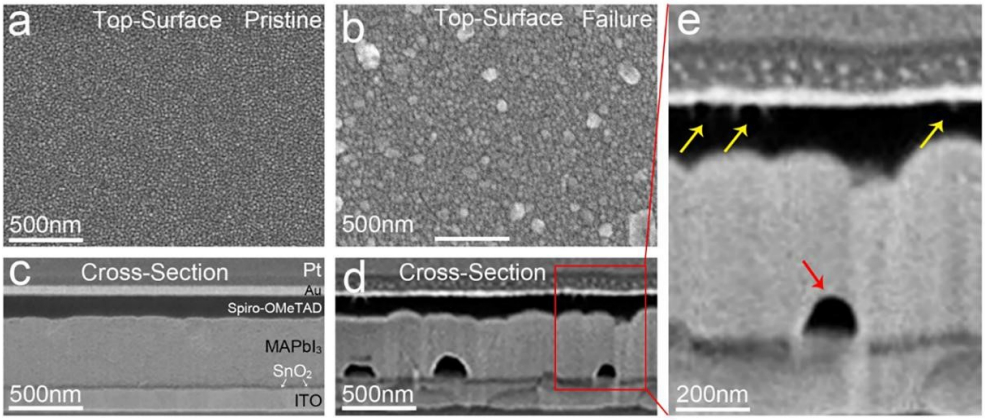

Fig. S12 Micro-structures of the PSC devices after heating treatment at 85 °C in N_2 gas (in dark) for different times. a, b) SEM images for the top surface morphology of the gold electrodes on the PSC devices before (as pristine) and after annealing 120 hours (as failure). **c, d)** SEM images of cross-sectional morphology of the pristine and the failure PSC device after thermal treatment for 120 hours, respectively. The thickness of the samples is larger than 2 um. **e)** Magnified SEM image for the cross-sectional morphology of PSC device in **d** (red square area). Yellow arrows indicate pinholes at the interface between Spiro-OMeTAD and gold electrode. Red arrow presents the fault at the $MAPbI_3$-SnO_2 interface.

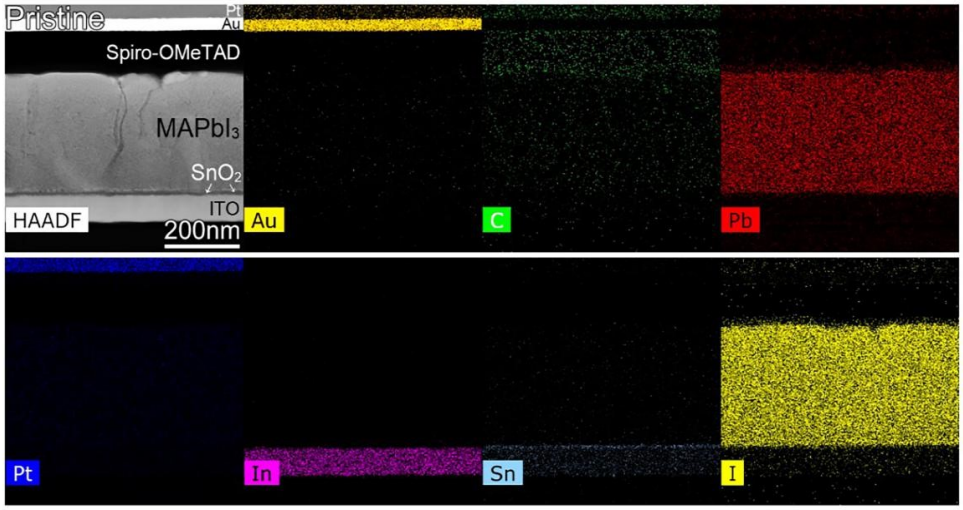

Fig. S13 The cross-sectional morphology and elementary distribution in the PSC device. High-angle annular dark-field (HAADF) image of the PSC and the corresponding EDS mapping of the Au, C, Pb, Pt, In, Sn and I elements in the PSC device. The thickness of the sample is about 0.25 um.

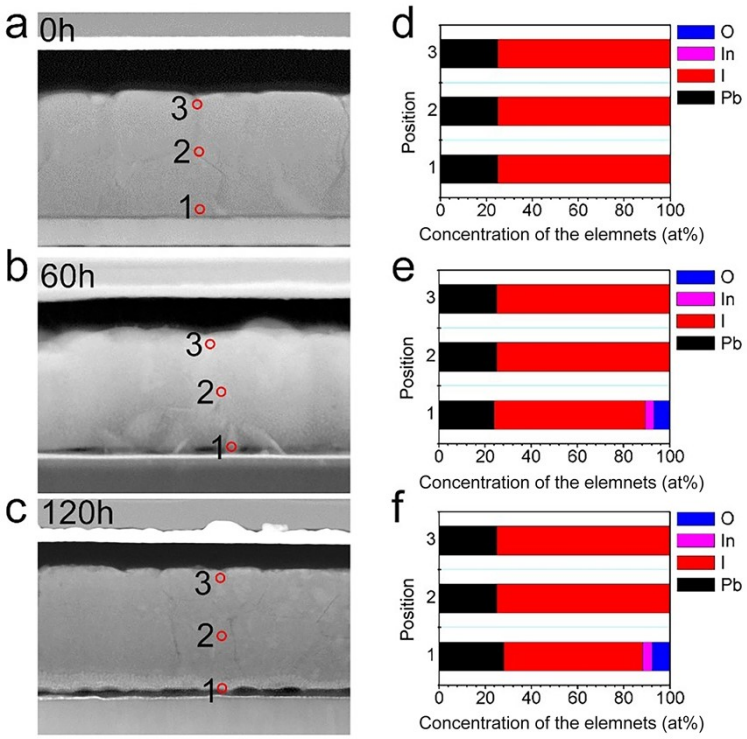

Fig. S14 Evolution for the morphology and elements in PSCs. a-c) HAADF images for the cross-section of annealed PSCs. **d-f)** the corresponding elementary distribution at the longitudinal direction of the annealed perovskite films. The thickness of the samples is about 0.25 um.

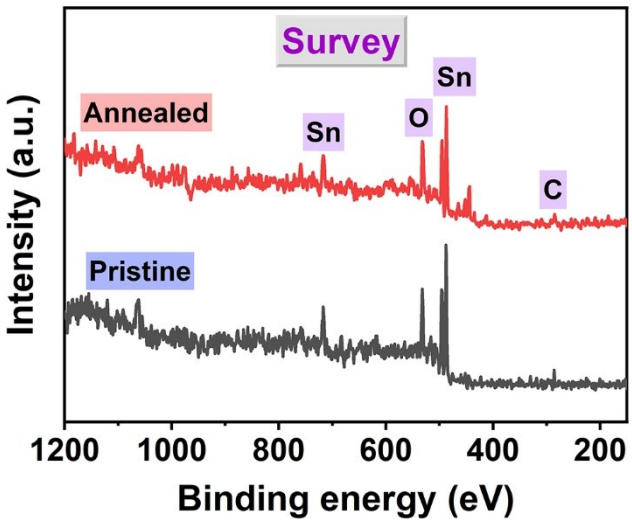

Fig. S15 The XPS survey spectra of pristine and annealed SnO_2 layers.

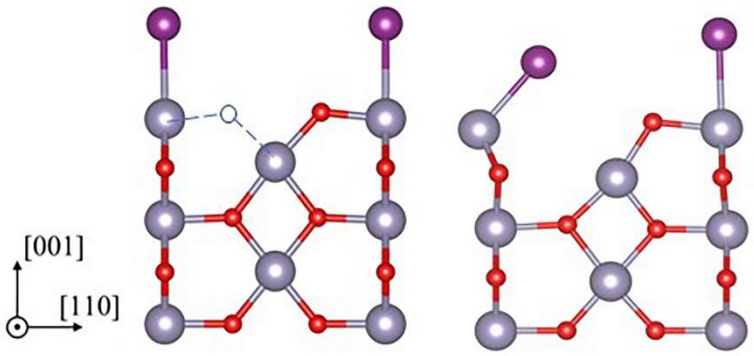

Fig. S16 The initial a) and final b) structures as removing oxygen atom to form a vacancy, corresponding to site-B in Fig. 4e**.** An oxygen atom was removed to form a vacancy near the interfaces. The neighboring I atom has been affected by moving toward to the SnO_2 slab by 0.81 Å.

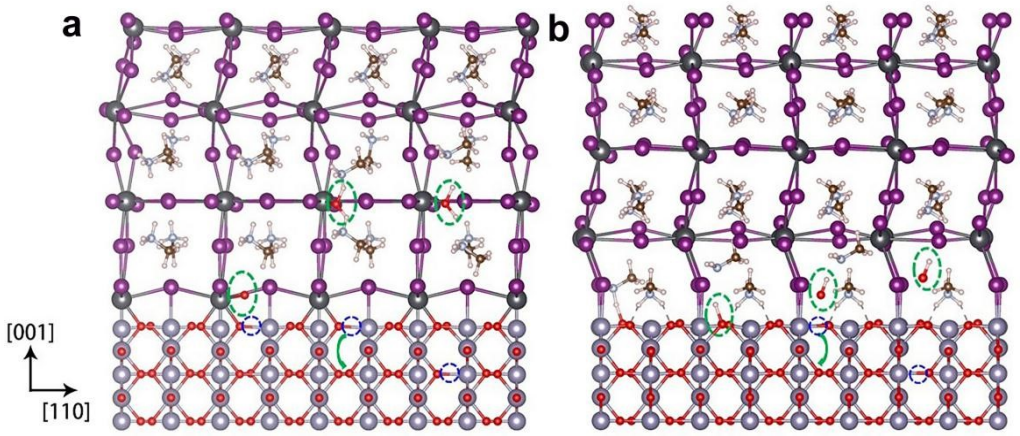

Fig. S17 Schematic diagram of the reaction process at the $MAPbI_3/SnO_2$ interface, for a) Pb-I terminated interface and for b) MA-I terminated interface. Dash blue circles present the oxygen vacancies, dash green ovals indicate the diffusion pathway of oxygen.

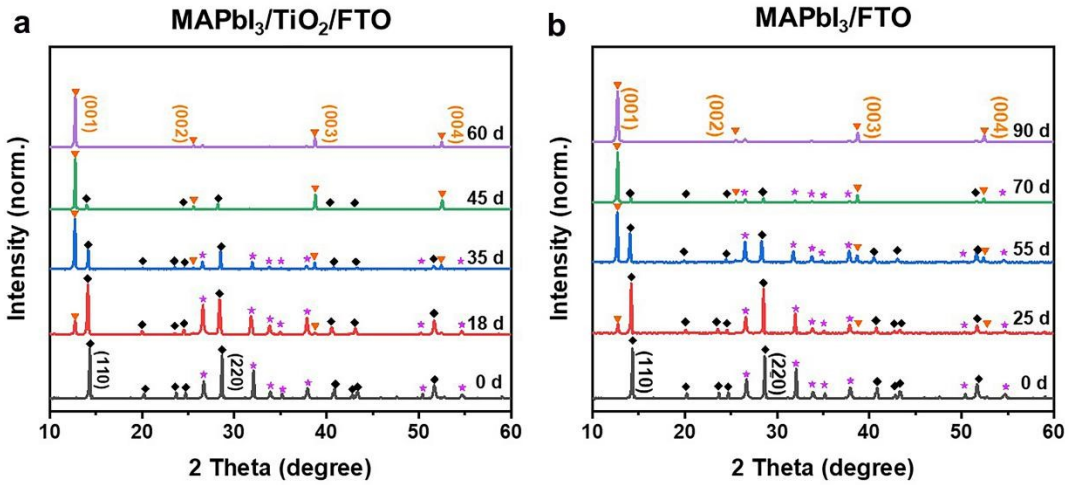

Fig. S18 X-Ray diffraction pattern analyses of the $MAPbI_3$ films on TiO_2-FTO and FTO substrates after thermal treatment for different times. The black indexes correspond to the structure of the tetragonal perovskite and the orange indexes correspond to the structure of lead iodide.

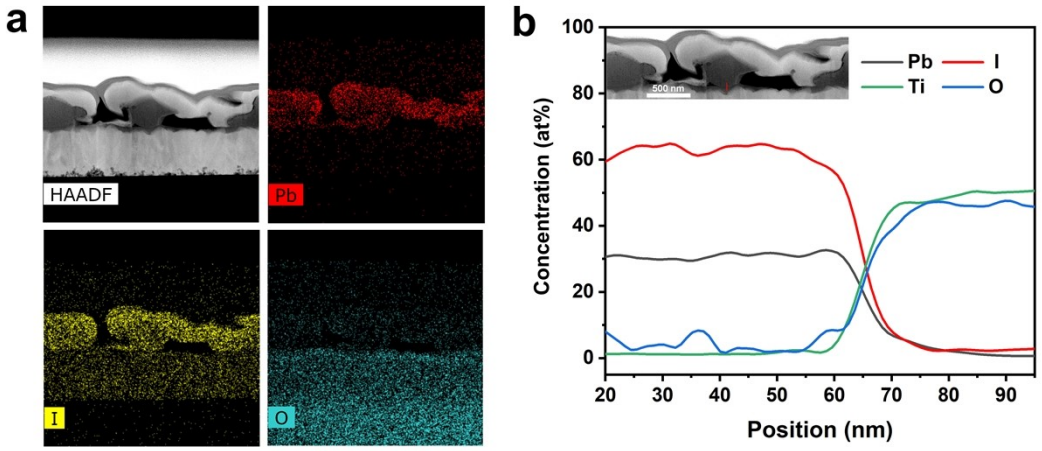

Fig. S19 The EDS mapping and line scan elementary distribution of the $MAPbI_3/TiO_2$/FTO sample after thermal treatment. a) EDS mapping reveals the elementary distribution on cross-sectional $MAPbI_3$ perovskite films, which is deposited on the TiO_2-FTO glass and thermally treated at 85 °C for 45 days. **b)** The EDS line scan of the elementary distribution along the red lines at the interfaces between $MAPbI_3$ and TiO_2 (inset shows the HAADF images of the detail interface, and line scan is selected at the red line area). The thickness of the sample is about 0.25 um.

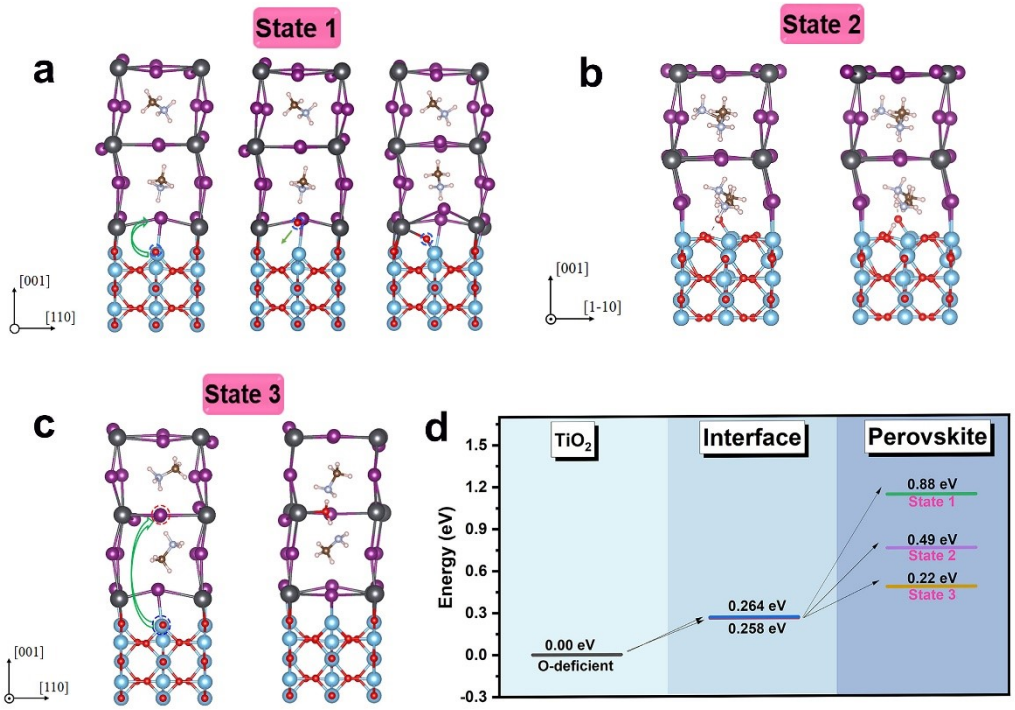

Fig. S20 a) The initial, intermediate, and final structures as one oxygen atom was released into the interfacial core. **b)** The structural changes after H is captured by the oxygen atom at the MAI/TiO_2 interfaces. **c)** The initial and relaxed structures for different layers as an iodine vacancy (red cycle for the iodine atom) was formed and an oxygen atom (blue cycle for the oxygen atom) at the interface diffused into the iodine vacancy. **d)** Diagram for the migration energy of oxygen from the oxygen-deficientTiO_2 surface into the different states of perovskite lattice.

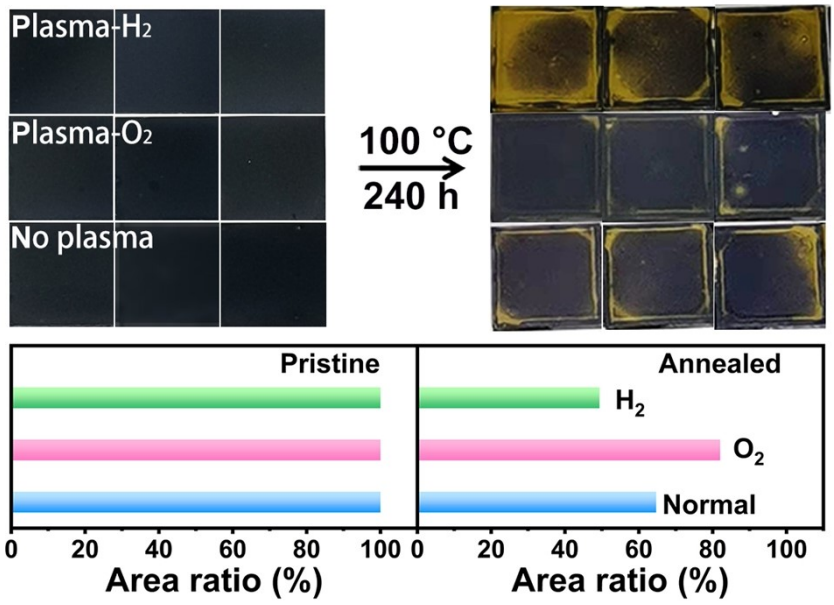

Fig. S21 Thermal stability of $FA_{0.9}Cs_{0.1}PbI_3$ films on the H_2, O_2 and no plasma treated SnO_2 layers. After annealing the perovskite films at 100 °C for 240 hours, the yellow phase of PbI_2 generates from the black phase of $FA_{0.9}Cs_{0.1}PbI_3$ films.

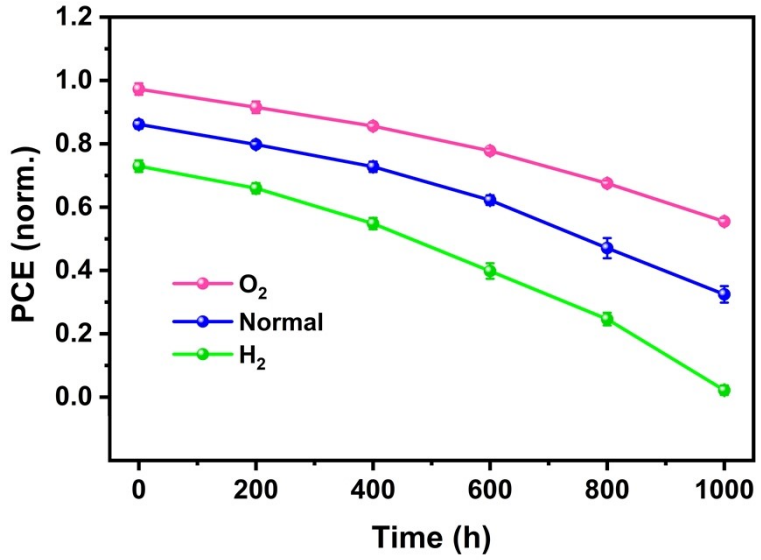

Fig. S22 Evolution for the normalized-PCE of $FA_{0.9}Cs_{0.1}PbI_3$-based PSCs was analyzed under the thermal annealing condition at 85 °C for different times, all the PSC devices were fabricated on different plasma treated SnO_2 layer.

Table S1 Calculated net atomic charges (NACs), sum of bond orders (SBOs), and vacancy formation energy (E_f^{yo}) at different sites (sites A-F) of SnO_2/perovskite interfaces.

	Site A	**Site B**	**Site C**	**Site D**	**Site E**	**Site F**
NAC	-0.89	-0.90	-0.96	-0.92	-0.89	-0.96
SBO	2.05	1.83	2.01	1.93	1.67	2.04
$^{a}E_f^{yo}$	3.18	1.72	1.91	2.20	1.66	2.21
$^{b}E_f^{yo}$	1.68	0.22	0.42	0.71	0.16	0.71

$^{a}E_f^{yo}$ and $^{b}E_f^{yo}$ indicates the vacancy formation energy in O-rich and O-poor SnO_2. The vacancy formation energy is much lower in the oxygen-poor SnO_2 layer ($^{b}E_f^{yo}$).

Table S2 Calculated E_f^{yo} at different sites (sites A-F) of TiO_2/perovskite interfaces.

	Site A	**Site B**	**Site C**	**Site D**	**Site E**	**Site F**
$^{c}E_f^{yo}$	3.54	2.62	2.89	2.68	2.85	3.11
$^{d}E_f^{yo}$	1.12	0.20	0.47	0.26	0.43	0.69

$^{c}E_f^{yo}$ and $^{d}E_f^{yo}$ indicates the vacancy formation energy in O-rich and O-poor TiO_2. The vacancy formation energy is much lower in the oxygen-poor TiO_2 layer ($^{d}E_f^{yo}$).

Table S3 The photovoltaic performance of V_{oc}, J_{sc}, FF and PCE of O_2-plasma treated $MAPbI_3$-based PSCs after thermal annealing at 85 °C for different time (each condition contains 10 samples).

	Time (h)	Voc (V)	Jsc (mA/cm^2)	FF (%)	PCE (%)
O_2	0	0.97±0.04	21.3±1.0	63.0±3.5	13.0±0.1
	6	1.00±0.03	21.5±1.0	66.8±4.0	14.4±0.1
	15	1.01±0.02	22.1±0.7	68.7±3.0	15.4±0.1
	24	0.98±0.04	19.9±1.9	66.8±3.5	12.8±0.1
	33	0.95±0.03	19.7±0.8	59.6±2.8	11.1±0.2
	48	0.94±0.03	18.5±1.0	57.6±3.0	10.0±0.1
	65	0.92±0.03	17.1±1.8	57.4±6.7	8.9±0.2
	80	0.90±0.05	16.7±3.1	56.9±11.1	8.3±0.1
	100	0.85±0.04	15.4±2.0	52.6±6.1	6.8±0.3
	120	0.73±0.04	6.1±0.7	43.5±4.9	1.9±0.3

Table S4 The photovoltaic performance of V_{oc}, J_{sc}, FF and PCE of normal $MAPbI_3$-based PSCs after thermal annealing at 85 °C for different time (each condition contains 10 samples).

	Time (h)	Voc (V)	Jsc (mA/cm^2)	FF (%)	PCE (%)
Normal	0	0.97±0.03	21.0±0.4	61.4±3.0	12.3±0.2
	6	0.98±0.03	21.4±0.7	64.3±2.8	13.5±0.2
	12	1.00±0.02	22.0±1.0	66.8±2.5	14.7±0.1
	24	0.98±0.04	19.6±1.2	60.7±4.8	11.6±0.1
	33	0.94±0.07	18.8±2.8	56.4±7.5	9.8±0.2
	48	0.93±0.05	17.7±2.5	53.2±8.9	8.6±0.3
	65	0.86±0.04	15.8±3.3	52.9±10.9	6.9±0.3
	80	0.86±0.12	14.8±4.4	50.8±12.9	6.0±0.3
	100	0.77±0.05	9.6±1.5	46.0±5.3	3.3±0.2
	120	0.73±0.04	6.1±0.7	43.5±4.9	1.9±0.3

Table S5 The photovoltaic performance of V_{oc}, J_{sc}, FF and PCE of H_2-plasma treated $MAPbI_3$-based PSCs after thermal annealing at 85 °C for different time (each condition contains 10 samples).

	Time (h)	Voc (V)	Jsc (mA/cm^2)	FF (%)	PCE (%)
H_2	0	0.95±0.05	19.7±1.2	61.2±2.8	11.5±0.3
	6	0.96±0.05	20.8±1.0	64.1±4.0	12.7±0.2
	10	0.97±0.03	21.3±0.7	65.4±2.4	13.6±0.2
	24	0.97±0.02	18.6±1.4	59.7±3.4	10.8±0.3
	33	0.92±0.04	17.6±2.8	53.1±9.8	8.4±0.2
	48	0.87±0.12	17.4±3.8	47.5±12.9	6.7±0.3
	65	0.80±0.22	14.9±4.4	44.8±13.7	4.6±0.4
	80	0.67±0.07	6.3±1.3	43.3±4.7	1.7±0.3

Table S6 The photovoltaic performance of open-circuit voltage (V_{oc}), current density (J_{sc}), fill factor (FF) and PCE of $FA_{0.9}Cs_{0.1}PbI_3$-based PSCs after thermal annealing at 85 °C for different time (each condition contains 10 samples). Here, the "O_2", "normal" and "H_2" indicates the PSCs fabricating on different plasma treated SnO_2 layers.

	Time (h)	Voc (V)	Jsc (mA/cm^2)	FF (%)	PCE (%)
O_2	0	1.03±0.04	23.4±0.6	71.7±3.6	18.0±0.2
	200	1.03±0.02	23.0±0.6	71.7±2.2	17.3±0.1
	400	1.02±0.01	22.4±0.4	71.5±2.1	16.4±0.1
	600	0.99±0.04	22.2±0.2	69.6±3.6	15.3±0.1
	800	0.99±0.02	21.8±1.3	64.8±3.8	13.9±0.1
	1000	0.98±0.03	20.6±1.5	61.8±5.3	12.3±0.2
Normal	0	1.02±0.02	22.5±0.3	71.4±2.4	16.5±0.2
	200	1.02±0.02	21.9±1.2	67.3±3.0	15.6±0.2
	400	0.99±0.04	21.8±0.6	67.0±3.2	14.7±0.2
	600	0.96±0.05	21.3±1.1	64.5±4.0	13.2±0.2
	800	0.93±0.05	21.7±1.1	57.7±4.7	11.1±0.4
	1000	0.91±0.03	18.5±1.7	54.7±5.3	9.1±0.4
H_2	0	0.99±0.04	22.1±1.1	66.3±2.9	14.7±0.2
	200	0.97±0.04	21.1±3.2	64.4±4.7	13.7±0.2
	400	0.97±0.04	20.5±1.4	61.7±5.0	12.2±0.2
	600	0.95±0.07	19.1±2.3	56.8±6.0	10.1±0.3
	800	0.89±0.01	13.5±1.0	54.0±6.6	8.1±0.3
	1000	0.84±0.03	11.2±1.6	53.5±11.4	5.0±0.2